Journal of Hydrology 585 (2020) 124828

Contents lists available at ScienceDirect

Journal of Hydrology

journal homepage: www.elsevier.com/locate/jhydrol

Research papers

Estimating snow depth by combining satellite data and ground-based observations over Alaska: A deep learning approach

Jiwen Wang[a], Qiangqiang Yuan[a,*], Huanfeng Shen[c,d,e], Tingting Liu[g,*], Tongwen Li[c], Linwei Yue[b], Xiaogang Shi[h], Liangpei Zhang[d,f]

[a] School of Geodesy and Geomatics, Wuhan University, Wuhan, Hubei 430079, China
[b] Faculty of Information Engineering, China University of Geosciences, Wuhan, Hubei 430079, China
[c] School of Resource and Environmental Sciences, Wuhan University, Wuhan, Hubei 430079, China
[d] The Collaborative Innovation Center for Geospatial Technology, Wuhan, Hubei 430079, China
[e] The Key Laboratory of Geographic Information System, Ministry of Education, Wuhan University, Wuhan, Hubei 430079, China
[f] The State Key Laboratory of Information Engineering in Surveying, Mapping and Remote Sensing, Wuhan University, Wuhan, Hubei 430079, China
[g] The Chinese Antarctic Center of Surveying and Mapping, Wuhan University, Wuhan, Hubei 430079, China
[h] University of Glasgow, Glasgow, Scotland G128QQ, United Kingdom

ARTICLE INFO

This manuscript was handled by Marco Borga, Editor-in-Chief, with the assistance of Luca Brocca, Associate Editor

Keywords:
Deep learning
Multisource data
GNSS-R
Brightness temperature
Alaska
Snow depth

ABSTRACT

Snow cover plays a vital role in the climate system because it is related to climate, hydrological cycle, and ecosystem. On this basis, deriving a long-term and large-scale snow depth (SD) time series and monitoring its temporal and spatial variations are crucial. Passive microwave remote sensing data in combination with in-situ SD data have long been used to retrieve SD. However, the retrieval accuracy is limited in case of sparse meteorological stations, and the high-quality applications of retrieval results are hindered in specific areas. The ground-based global navigation satellite system reflectometry (GNSS-R) method is currently a potential way to monitor SD variations with a high degree of accuracy but has a limited spatial coverage. In this study, a deep learning-based approach, which displays a stronger nonlinear expressiveness capability than conventional neural networks, was applied to estimate SD by combining satellite observations, in-situ data, and GNSS-R estimates. The model was trained and tested with data obtained in Alaska between 2008 and 2017. Results show that the proposed deep belief network model performs better than linear methods and conventional neural network models and demonstrate the effectiveness of combining GNSS-R estimation with increased cross-validation R of 0.85 and decreased RMSE of 15.40 cm. The predicted SD distribution indicates that the variations in mean SD in Alaska for March and April between 2008 and 2017 were associated with the climate anomalies and air temperature. Overall, the proposed deep learning-based method is a promising approach in the satellite-retrieved SD field.

1. Introduction

Snow is a crucial component of a climate system and directly affects the energy balance of the Earth's surface due to its heat-insulation effect and high albedo (Che et al., 2016; Dietz et al., 2012; Wu et al., 2018). Snow also plays a prominent role in the water cycle, and snowmelt runoff is a stable and reliable water source in many water-scarce regions (Kang et al., 2014; Shi et al., 2015; Tedesco et al., 2015; Wang et al., 2015). Extensive and continuous snow can also cause natural disasters, such as avalanches, which can lead to considerable loss of life and property. Snow depth (SD) data can provide quantitative information about the material and energy of snow. Thus, obtaining accurate SD information is crucial for the research on climatology and hydrology.

Conventional SD measurement methods can measure SD through in-situ devices with a high degree of accuracy (Rasmussen et al., 2012). However, these methods cannot capture the spatiotemporal SD variation characteristics under sparse distribution of observation stations. Over the past four decades, passive microwave (PM) remote sensing has exhibited the ability to acquire long-term and large-scale SD datasets with the rapid evolution of satellite remote sensing (Armstrong and Brodzik, 2002; Liu et al., 2018; Rostosky et al., 2018). PM remote

---

* Corresponding authors.

E-mail addresses: wangjiwen@whu.edu.cn (J. Wang), qqyuan@sgg.whu.edu.cn (Q. Yuan), shenhf@whu.edu.cn (H. Shen), ttliu23@whu.edu.cn (T. Liu), litw@whu.edu.cn (T. Li), yuelw@cug.edu.cn (L. Yue), John.Shi@glasgow.ac.uk (X. Shi), zlp62@whu.edu.cn (L. Zhang).

https://doi.org/10.1016/j.jhydrol.2020.124828
Received 1 December 2019; Received in revised form 17 February 2020; Accepted 10 March 2020

sensing has become an effective way to estimate SD given that it can provide all-day and all-weather monitoring and spatially continuous information of SD variation with high temporal resolution (Gu et al., 2014; Li et al., 2019).

PM remote sensing observation is based on the assumption that the electromagnetic radiation characteristics of snow have a strong dependence on SD (Rosenfeld and Grody, 2000). In snow-covered areas, the microwave radiometer carried by a satellite records the microwave radiation energy from the ground in the form of brightness temperature (Tb), which includes two main components: one is the radiation from the snow cover, and the other is that from the ground beneath. The brightness temperature decreases with the increase in SD because of the volume scattering of snow particles (Dai et al., 2012; Mashtayeva et al., 2016). The scattering effect is directly proportional to the microwave frequency; thus, the brightness temperature of the high-frequency channel is lower than that of the low-frequency channel (Shi et al., 2016; Ulaby and Stiles, 1980). Therefore, SD retrieval based on PM remote sensing is often to establish the functional relationship between SD and brightness temperature.

Several algorithms have been developed to estimate SD by combining remote sensing data and station observations. The most common method is to establish the linear relationship between SD and brightness temperature by utilizing the difference between the horizontally polarized brightness temperatures of 19 and 37 GHz and the ground-measured SD. In many studies, Chang algorithm (Chang et al., 1987) has been modified by considering the parameters that affect the SD retrieval accuracy, such as forest and terrain (Foster et al., 1997; Langlois et al., 2011). However, linear methods cannot exactly describe the nonlinear relationship between SD and brightness temperature and tend to underestimate SD (Gan et al., 2013). Therefore, nonlinear methods, such as artificial neural networks (ANNs), have emerged to establish the nonlinear relationship between the input variables (brightness temperature and auxiliary data) and SD. For instance, ANNs have been trained to retrieve SD by combining in-situ measurements and brightness temperatures observed by using PM sensors (Cao et al., 2008; Santi et al., 2012; Tabari et al., 2010; Tedesco et al., 2004). ANNs have also been trained with model simulations for the estimation of SD (Chang and Tsang, 1992; Davis et al., 1993; Tedesco et al., 2004). Brightness temperatures are simulated on the basis of radiative transfer model by using some snow properties, and the simulated brightness temperature and SD are taken as the input and output of ANN models, respectively. Moreover, some auxiliary parameters (e.g., forest cover fraction, and elevation) have been regarded as input parameters of ANN models to improve the retrieval accuracy under the influence of forest and terrain (Bair et al., 2018; Evora et al., 2008; Gan et al., 2009). Santi et al. (2014) used AMSR-E equivalent brightness temperature corrected for the effects of orography and forest coverage instead of the original brightness temperature as inputs of ANN model to estimate SD and demonstrated the improvement of retrieval accuracy. These nonlinear methods have shown great advantages in estimating SD and have higher precision than linear methods.

The ground-based global navigation satellite system reflectometry (GNSS-R) method is currently a new way of monitoring SD variation at the spatial scale of approximately 1000 m^2, which is larger than the spatial scale of in-situ measurements, with high temporal and spatial resolution. Larson et al. (2009) first estimated SD on the basis of signal-to-noise ratio (SNR) because the multipath reflection component of the SNR observations is associated with SD. The reliability and accuracy of the SNR-based method have been proven at sites with three land cover types (Nievinski and Larson, 2014). Tabibi et al. (2017) analyzed the SD estimated using different frequency bands of global positioning system (GPS) and GLONASS and found that accurate results can be obtained using GPS L2C and GLONASS SNR observations. The solutions of SD measurement in different interference environments have been proposed to address the signal interference problem of SNR-based methods in complex terrain environment by analyzing the interference factors (Vey et al., 2016; Zhang et al., 2017). A GNSS-R network (PBO H2O network) based on GNSS stations has also been developed on the western coast of the USA and Alaska (Larson and Nievinski, 2013), where GNSS-R SD is directly available through open access. The accuracy of the GNSS-R SD product has been validated and has shown a precision of a few centimeters (Larson and Nievinski, 2013; McCreight et al., 2014). The GNSS-R product from PBO H2O network has been used as the true value of SD to validate other SD products (Boniface et al., 2015). In summary, the GNSS-R method not only can monitor SD with the advantage of an all-day and all-weather ability but also can estimate SD with a high degree of accuracy. However, GNSS-R observation is also restricted to a limited spatial scale, and GNSS-R stations are sparsely distributed.

Deep learning, which displays a stronger nonlinear expressiveness capability than conventional neural networks, has achieved great success in geoscience inversion, including fine particulate matter (Li et al., 2017) and soil moisture (Jia et al., 2019; Song et al., 2016). However, deep learning has rarely been applied to retrieve SD to date. Thus, this study aimed to establish a deep learning-based model for estimating SD. However, the sparsely distributed samples from combining only satellite and sparsely distributed in-situ observations may limit the accuracy of SD retrieval. In this study, the SDs estimated by the GNSS-R method were taken as true values and combined with in-situ observations to increase the station density of the sample data for the following two reasons: one is that the accuracy of the GNSS-R method in SD retrieval is high, and the other is that the spatial scale of the GNSS-R technique (nearly 1000 m^2) is better than the point-scale (< 1 m^2) in-situ measurements (Xu et al., 2018) in terms of brightness temperature data. Therefore, the proposed deep learning-based SD retrieval model was constructed and evaluated on the basis of the combination of satellite observations, in-situ data, and GNSS-R estimation. Alaska was selected as the study region because it has an abundance of snow and has a mature GNSS-R SD product that is available through open access by connecting to the PBO H2O network.

The remainder of the paper is organized as follows. In Section 2, the study region and data used are described. Section 3 introduces the deep learning-based SD retrieval method, that is, the deep belief network (DBN) model developed here, and the indicators used for the evaluation. In Section 4, the performance evaluation of this model against daily ground-measured SD data are described, and we compare the results with those of four other SD retrieval models, namely, Chang, multiple linear regression (MLR), back propagation neural network (BPNN), and generalized regression neural network (GRNN). The former two are linear models, and the latter two are nonlinear ones. On the basis of the derived SD distribution from 2008 to 2017, we analyze the variation in SD in Alaska over this time period and its response to climate anomalies and air temperature. Finally, our work is summarized in Section 5.

2. Study region and data

2.1. Study region

Alaska, which is in the latitude and longitude range of 54°N–71°N and 130°W–173°W, was chosen as the study region (Fig. 1). The study period was from 2008 to 2017. Alaska is located at high latitudes. Thus, most parts of this region are cold all year round. Alaska experiences abundant precipitation as a result of being surrounded by three oceans (the North Pacific Ocean, the Bering Sea, and the Arctic Ocean). Therefore, this region has an abundance of snow cover. Typically, north Alaska has a polar cold and dry climate with the air temperature below zero all year round. Central Alaska has a continental climate with an average annual temperature of -2.47 °C and an average annual precipitation of 275 mm at Fairbanks, while southern Alaska has a temperate maritime climate with an average temperature of 3.7 °C and an average annual precipitation of 617 mm at Homer. Mature GNSS-R SD

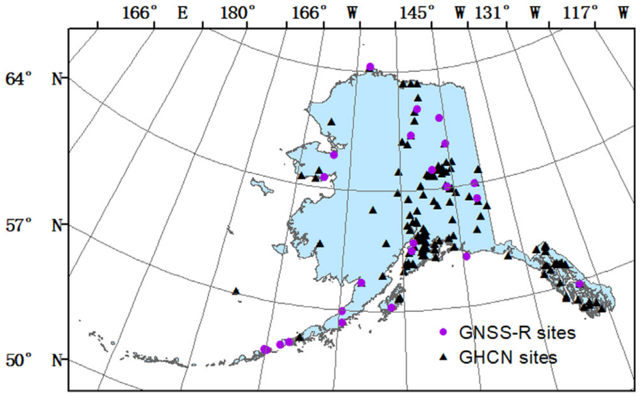

Fig. 1. Study area and the distribution of Global Historical Climate Network (GHCN) and Global Navigation Satellite System Reflectometry (GNSS-R) stations. The blue area represents the region of Alaska. (For interpretation of the references to colour in this figure legend, the reader is referred to the web version of this article.)

products, as well as conventional in-situ and satellite observations, are available in Alaska. The above-mentioned considerations indicate that Alaska is ideal for the research on snow cover using integrated multi-source data.

2.2. Data

2.2.1. Satellite observations

The Special Sensor Microwave Imager/Sounder (SSMIS) is a satellite-borne microwave radiometer onboard the U.S. Defense Meteorological Satellite Program F17. The brightness temperature data observed by SSMIS gridded to the EASE-Grid with daily temporal resolution and 25 km spatial resolution (Armstrong et al., 1994; Brodzik, 2002) have been available at the National Snow and Ice Data Center (https://nsidc.org/) since December 2006 and contain four frequencies, namely, 19, 22, 37, and 91 GHz. Except for 22 GHz, which is only vertically polarized (i.e., Tb22V), the other frequencies have horizontal and vertical polarization modes (i.e., Tb19H, Tb19V, Tb37H, Tb37V, Tb91H, and Tb91V.). Thus, seven channels of brightness temperature are available. The daily SSMIS brightness temperature data from 2008 to 2017 were downloaded from the National Snow and Ice Data Center. In this study, descending overpass observations (during early morning) were used given that liquid water could be existing in the snow during the afternoon satellite overpass and the SD could not be retrieved in the case of wet snow (Che et al., 2008; Kelly and Chang, 2003).

2.2.2. In-situ SD

The Global Historical Climate Network (GHCN, https://www.ncdc.noaa.gov/snow-and-ice/) integrates daily climate datasets from meteorological stations around the world and provides in-situ SD datasets for daily temporal resolution. The daily SD datasets include the information of location, measuring time, and SD. Daily in-situ SD data of 155 sites within the study region from 2008 to 2017 were obtained from GHCN and utilized for the construction and performance evaluation of the SD retrieval model (Tsutsui and Maeda, 2017).

2.2.3. GNSS-R estimation

The daily GNSS-R SD product data can be obtained from the PBO H2O Data Portal (https://gnssh2o.jpl.nasa.gov/index.php?product=snow), which uses a traditional geodetic GPS signal-receiving station to monitor the change in SNR for long time series and then estimates the SD based on GNSS-R with a high precision of a few centimeters (Larson et al., 2009; Larson and Nievinski, 2013). A total of 25 GNSS-R stations are present in Alaska (Fig. 1), and the daily GNSS-R SD data from 2008 to 2017 were taken as the actual SD, together with the in-situ measurements, to establish and evaluate the SD retrieval model.

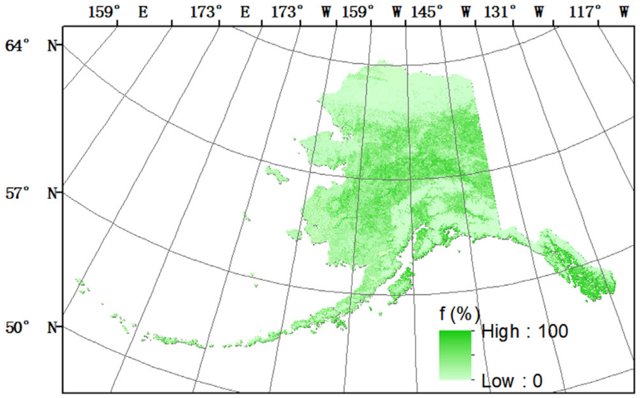

Fig. 2. Distribution of the forest cover fraction for 2008 as an example.

2.2.4. Forest cover fraction data

Forest cover fraction data were also used considering the potential impact of forest on SD retrieval. The MOD44B Version 6 Vegetation Continuous Fields (VCF) product is a global representation of surface vegetation cover that can continuously and quantitatively portray land-surface cover at a pixel resolution of 250 m. Forest cover fraction data (Fig. 2) were obtained from the MOD44B MODIS/Terra VCF Yearly L3 Global 250 m SIN Grid V006 product (https://ladsweb.modaps.eosdis.nasa.gov/search/order/1/MOD44B–6).

2.2.5. Topographic data

Elevation parameter was utilized as auxiliary data to consider the effect of topographic parameters on the SD retrieval accuracy. The ETOPO1 Global Relief Model was used as elevation data, and its spatial resolution is 1 arc minute or approximately 2 km (Amante and Eakins, 2009). These model data (Fig. 3) can be downloaded from http://www.Ngdc.noaa.gov/mgg/global/.

2.3. Data matching and processing

First, the elevation and forest cover fraction data were regridded to the EASE-Grid, and the mean values of the forest cover fraction and elevation were calculated for the corresponding EASE-Grid to match the brightness temperature data. In addition, the SD data from multiple in-situ and GNSS-R stations were averaged for each EASE-Grid. Then, SD measurements from GHCN and PBO H2O network were associated with the satellite observations and ancillary data.

Second, we applied Grody's decision tree method (Che et al., 2008; Grody and Basist, 1996) to distinguish snow from other scattering signals given the resemblance of the microwave radiation characteristic of snow to that of frozen ground, cold desert, and precipitation (Table 1).

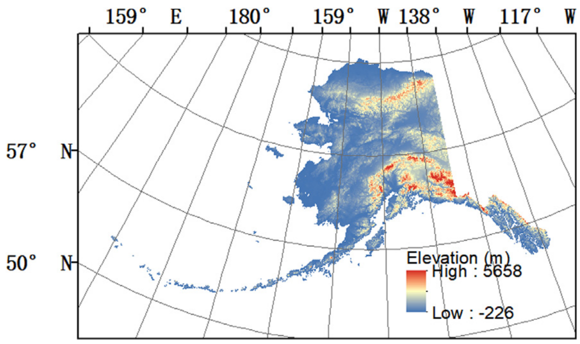

Fig. 3. Elevation variation in Alaska.

Table 1
Conditions for removing other scattering signatures.

Steps	Conditions
Scattering signature	Tb19V-Tb37V > 0 K
Precipitation	Tb22V > 258 K or 258 K ≥ Tb22V ≥ 254 K and Tb19V-Tb37V ≤ 2 K
Cold deserts	Tb19V-Tb19H ≥ 18 K and Tb19V-Tb37V ≤ 10 K
Frozen ground	Tb19V-Tb19H ≥ 8 K and Tb19V-Tb37V ≤ 2 K

Considering the hindering effect of wet snow on the SD retrieval based on PM remote sensing, the following dry snow criteria (Singh and Gan, 2000; Xiao et al., 2018) were applied to remove wet snow for ensuring high accuracy of SD retrieval:

$$\mathrm{Tb37V} < 250\mathrm{K}$$

$$\mathrm{Tb19V} - \mathrm{Tb37V} \geq 9\mathrm{K}$$

$$\mathrm{Tb37V} - \mathrm{Tb37H} \geq 10\mathrm{K}$$

$$P_{factor} = \frac{Tb37V - Tb37H}{Tb37V + Tb37H}, P_{factor} > 0.026 \tag{1}$$

Following the above-mentioned steps, wet snow and other scattering signals were excluded, and 11,447 dry snow samples were identified.

3. Methodology

3.1. Structure of the DBN model

The DBN model proposed in 2006 is a typical deep learning model (Hinton et al., 2006). The model can be utilized to solve prediction and classification problems (Chen et al., 2015; Huang et al., 2014). Consequently, the SD retrieval model in this study was established on the basis of DBN model.

The DBN model is composed of a back propagation (BP) layer and several restricted Boltzmann machine (RBM) layers. For instance, Fig. 4 shows the structure of a DBN model with two RBM layers. An RBM is made up of a visible layer (v) used to input training data and a hidden layer (h) used to extract data features, with the visible and hidden layers being bidirectionally linked. The first RBM's hidden layer is the second RBM's visible layer.

The training process for a DBN model consists of two main steps. The first step is to train the RBMs. When data are transmitted from v to h in the first RBM, the opening probability of every neuron in the hidden layer can be calculated according to Eq. (2):

$$p(h_j{=}1|v) = \sigma\left(\sum_{i=1}^{m} \omega_{ij} v_i + c_j\right) \tag{2}$$

where i and j respectively indicate the number of the ith visible neuron and the jth hidden neuron. ω_{ij} denotes the weight between visible neuron i and hidden neuron j, while $c_j$refers to the bias of the jth hidden neuron. Sigmoid function $\sigma()$ acts as the transfer function.

The calculated opening probability of each hidden neuron is compared with the random value μ extracted from the 0,1 uniform distribution, and the hidden neurons are updated to 0 or 1 in accordance with Eq. (3):

$$h_j = \begin{cases} 1, \ p(h_j = 1|v) \geq \mu \\ 0, \ p(h_j{=}1|v) < \mu \end{cases} \mu \ U(0, 1) \tag{3}$$

So is the calculation process from hidden layer to visible layer. In general, the contrastive divergence algorithm (Hinton and Salakhutdinov, 2006) is utilized to train an RBM. The neurons' weights and bias are then updated as the following formula until v is approximately equal to $v1$:

$$\begin{aligned} \omega &= \omega + \varepsilon\bullet((h)^T v - (h1)^T v1) \\ b &= b + \varepsilon\bullet(v - v1) \\ c &= c + \varepsilon\bullet((h)^T v - (h1)^T v1) \end{aligned} \tag{4}$$

where ε refers to the learning rate; h, $h1$ are obtained from v, $v1$ using Eqs. (2) and (3); $v1$ is reconstructed from the hidden layer (h); and b and c respectively indicate the bias for the visible and hidden neurons.

The RBMs are pretrained one after another without supervision, and the weights obtained through this unsupervised pretraining are used to initialize the multilayer network. The second step of the training process of the DBN is to fine-tune the coefficients between layers using a supervised BP algorithm.

3.2. SD retrieval model based on a DBN

In our case, the DBN model is adopted to learn the relationship between the input variables and SD through learning from the sample datasets:

$$SD = g(Tb19H, Tb19V, Tb37H, Tb37V, lat, lon, elevation, f, time) \tag{5}$$

where $g()$means the estimation function; lat, lon, and $elevation$represent 3D localization; and f indicates the forest cover fraction.

Fig. 5 shows the schematic of the DBN model used to retrieve SD. The input variables are PM horizontal and vertical polarization brightness temperatures of 19 and 37 GHz, latitude, longitude, elevation, forest cover fraction, and time. We apply two hidden layers (two

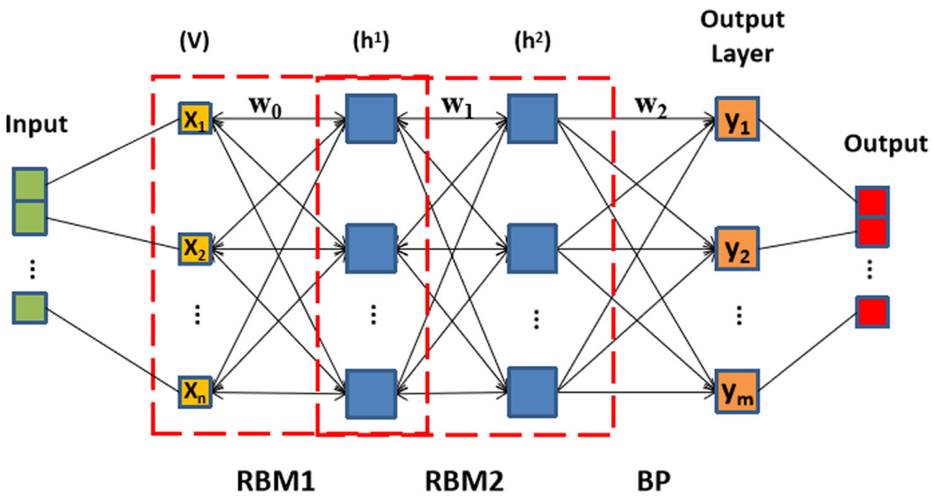

Fig. 4. Structure of the DBN model.

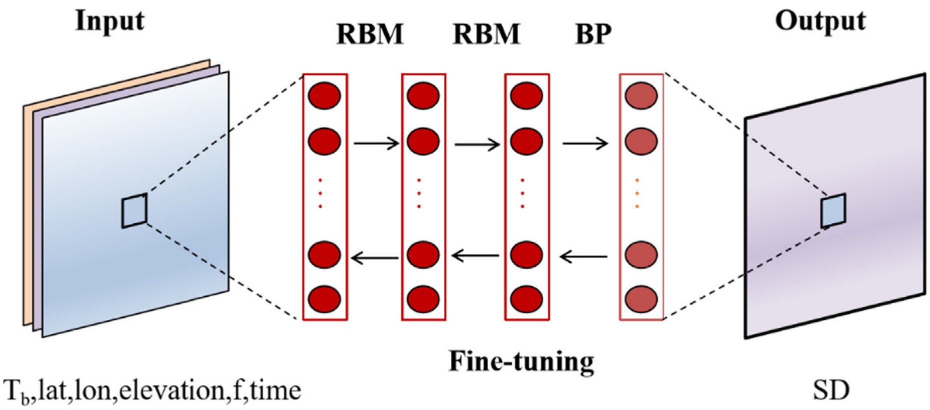

Fig. 5. Structure of the DBN model for SD modeling.

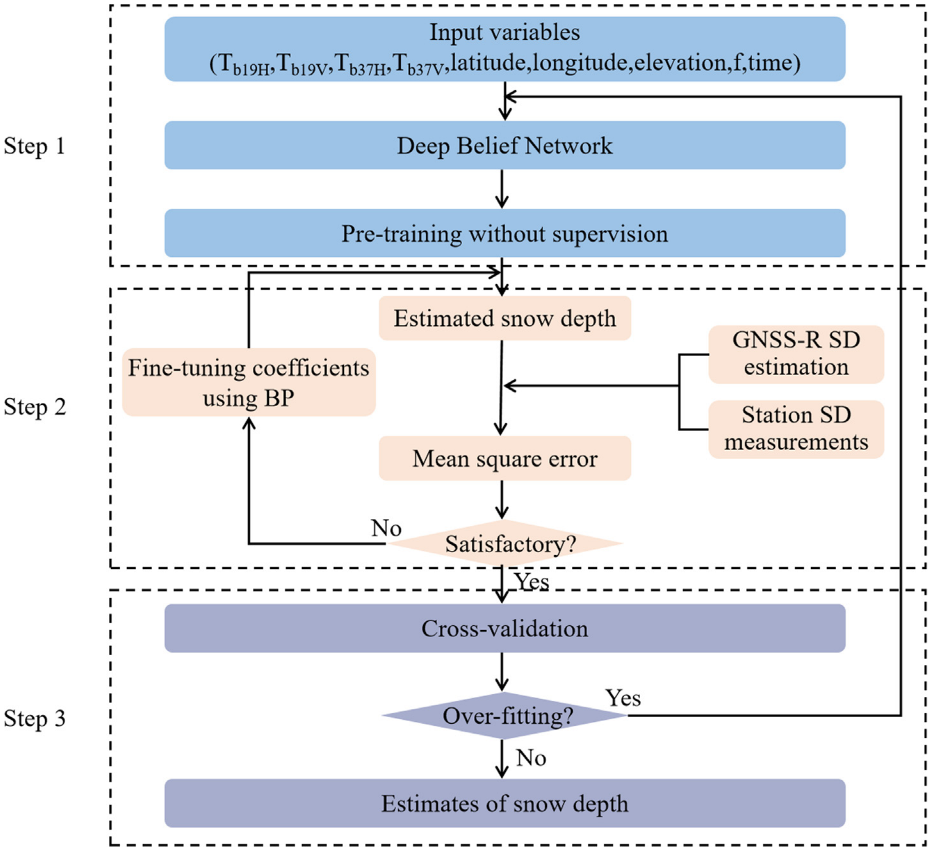

Fig. 6. Flowchart of the DBN model for SD modeling.

RBMs), where the amount of neurons in every hidden layer is 16. Following the two RBMs is a BP layer with one neuron (SD).

The specific process of the DBN model for SD modeling consists of three steps, as shown in Fig. 6.

First, the variables of horizontal and vertical polarimetric brightness temperatures of 19 and 37 GHz, latitude, longitude, elevation, forest cover fraction, and time are input into the model. In this step, only the input data are used to pretrain the DBN model, which indicates that the initial coefficients of this model are trained from input data. Meanwhile, actual SD is not utilized for tuning the coefficients in such process.

Second, we can estimate the SD value from the DBN model. Subsequently, the mean-square error (MSE) between the actual and retrieved SD is calculated and returned to fine-tune the coefficients of the model by utilizing the BP algorithm (Rumelhart et al., 1988). This procedure is repeated until the DBN model achieves a satisfactory performance. Then, the relationship between SD and satellite brightness temperature can be effectively established through this step.

Finally, this model is validated and then applied to estimate the SD where no ground stations exist. Accordingly, we can acquire the spatially continuous distribution of the SD.

We used three statistical indicators, namely, the correlation coefficient (R), the mean absolute error (MAE, cm), and the root-mean-square error (RMSE, cm), to quantitatively evaluate the model performance. We adopted a 10-fold cross-validation technique to test the over-fitting and predictive power of the model (Rodriguez et al., 2010). All the sample data were divided into 10 subsets equally and randomly. One of the subsets was selected as validation samples in turn, while the others were utilized for model fitting. Then, 10 results were averaged to evaluate the performance of the DBN model. Small differences between the model fitting and cross-validation statistics suggest non-overfitting (Hu et al., 2013). In addition, among the 10 models, the one which performed best, with the highest validation R, the lowest validation MAE, and the lowest validation RMSE, was selected to retrieve SD over the whole of Alaska.

3.3. Other SD retrieval algorithms for comparison

BPNN (Rumelhart et al., 1988; Tedesco et al., 2004), GRNN (Specht, 1991), Chang algorithm (Chang et al., 1987), and MLR (Xiao et al., 2018) were utilized to construct SD retrieval models on the basis of the same samples used by the DBN model for better assessing the performance of the deep learning-based SD retrieval model. The performances of these methods were compared with those of the DBN model.

3.3.1. Linear methods

Chang algorithm is a linear method used to estimate SD through performing linear regression for the difference in the brightness temperature using 18 and 36 GHz horizontal polarization and SD.

$$SD = 1.59 * (Tb18H - Tb36H) \tag{6}$$

where SD is estimated in centimeters. Tb18H and Tb36H denote the horizontal polarization brightness temperatures of 18 and 36 GHz, which were replaced with SSMIS horizontal polarization brightness temperatures of 19 and 37 GHz in this study (Xiao et al., 2018).

In addition, an SD retrieval model based on the MLR method was established using nine parameters (the same as the DBN model) for predicting SD.

$$SD = \alpha_0 + \alpha_1 \bullet lat + \alpha_2 \bullet lon + \alpha_3 \bullet elevation + \alpha_4 \bullet Tb19H + \alpha_5 \bullet Tb19V + \alpha_6 \bullet Tb37H + \alpha_7 \bullet Tb37V + \alpha_8 \bullet f + \alpha_9 \bullet time \tag{7}$$

3.3.2. Nonlinear method

As with the DBN model, BPNN and GRNN are data-driven learning models. The same input and output parameters were again used in the two neural networks. However, the BPNN model (Fig. 7a) has a relatively simple structure with three layers (input, hidden, and output layers), and the GRNN model (Fig. 7b) uses several hidden layer neurons to achieve function approximation. Instead, the DBN model not only has a more complex structure but also initializes through unsupervised pretraining.

4. Results and analysis

4.1. Evaluation of model performance

4.1.1. Performance of DBN modeling

Primarily, remote sensing data, auxiliary data, and in-situ observations were integrated to generate the sample datasets for the DBN model and the four alternative methods mentioned above. As presented in Table 2, the two kinds of linear methods, namely, Chang algorithm and the MLR method, perform the worst (cross-validation R of 0.15/0.47, MAE of 22.33/19.12 cm, and RMSE of 35.36/26.91 cm) as expected owing to that the nonlinear relationship between SD and brightness temperature is described as linear. In consideration of the nonlinear relationship between the input variables and SD, BPNN and GRNN perform better than the linear models (cross-validation R of 0.78/0.68, MAE of 12.80/15.17 cm, and RMSE of 19.01/22.33 cm). The DBN model, which is a complex learning model, can better fit the nonlinear relationship and obtains the best performance (cross-validation R of 0.81, MAE of 11.15 cm, and RMSE of 17.96 cm) among the other models.

Fig. 8 presents the scatter plots of actual SD and estimated value retrieved by the five algorithms. The underestimates and overestimates of SD retrieved by the DBN model are less than those of the GRNN and BPNN models, as presented in Fig. 8e, c, and d. These results demonstrate that the proposed deep learning-based SD retrieval model with a more complicated structure and a layer-by-layer unsupervised pretraining technique can estimate SD with a higher degree of accuracy. The two linear methods, as shown in Fig. 8a and b, tend to underestimate SD when the actual SD value exceeds 50 cm. This phenomenon can be due to the saturation of the difference in the brightness temperature. The results of MLR are better than those of Chang algorithm. This result may be due to that more parameters that correspond to snow properties are used in MLR.

The SD retrieval models in this section were established without combining the high-precision GNSS-R estimates. Thus, we used high-precision GNSS-R estimates as independent evaluation data to validate the retrieval accuracy of the DBN model and four other models for further verifying whether the DBN model performs best among the five compared methods. Fig. 9 shows the scatter plots of GNSS-R SD and estimated values retrieved by the five algorithms. The performances of the two linear methods remain the worst (validation R of 0.45/0.56). Although the MLR method can consider more parameters, it cannot map the complex nonlinear relationship between input parameters and SD. On the contrary, GRNN and BPNN can fit this nonlinear relationship and perform better than linear methods with validation R of 0.64/0.69. Furthermore, the DBN model remains the best-performing model with

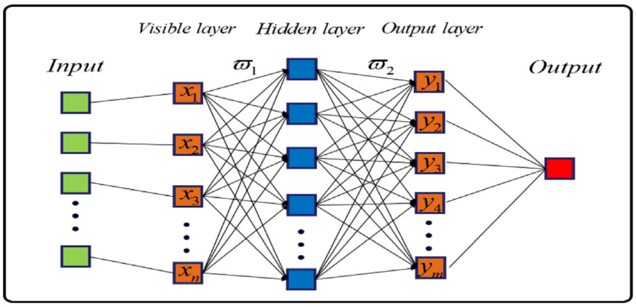

(a) BPNN

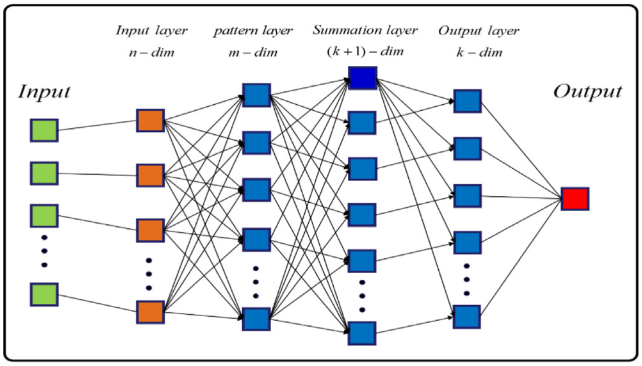

(b) GRNN

Fig. 7. Structure of the (a) BPNN model and (b) GRNN model.

Table 2
Model fitting and cross-validation performance of the models using satellite and GHCN observations.

Method	Model fitting			Cross-validation		
	R	MAE	RMSE	R	MAE	RMSE
Chang				0.15	22.33	35.36
MLR	0.47	19.15	26.94	0.47	19.12	26.91
GRNN	0.70	14.67	21.60	0.68	15.17	22.33
BPNN	0.81	11.56	18.05	0.78	12.80	19.01
DBN	0.83	10.16	17.18	0.81	11.15	17.96

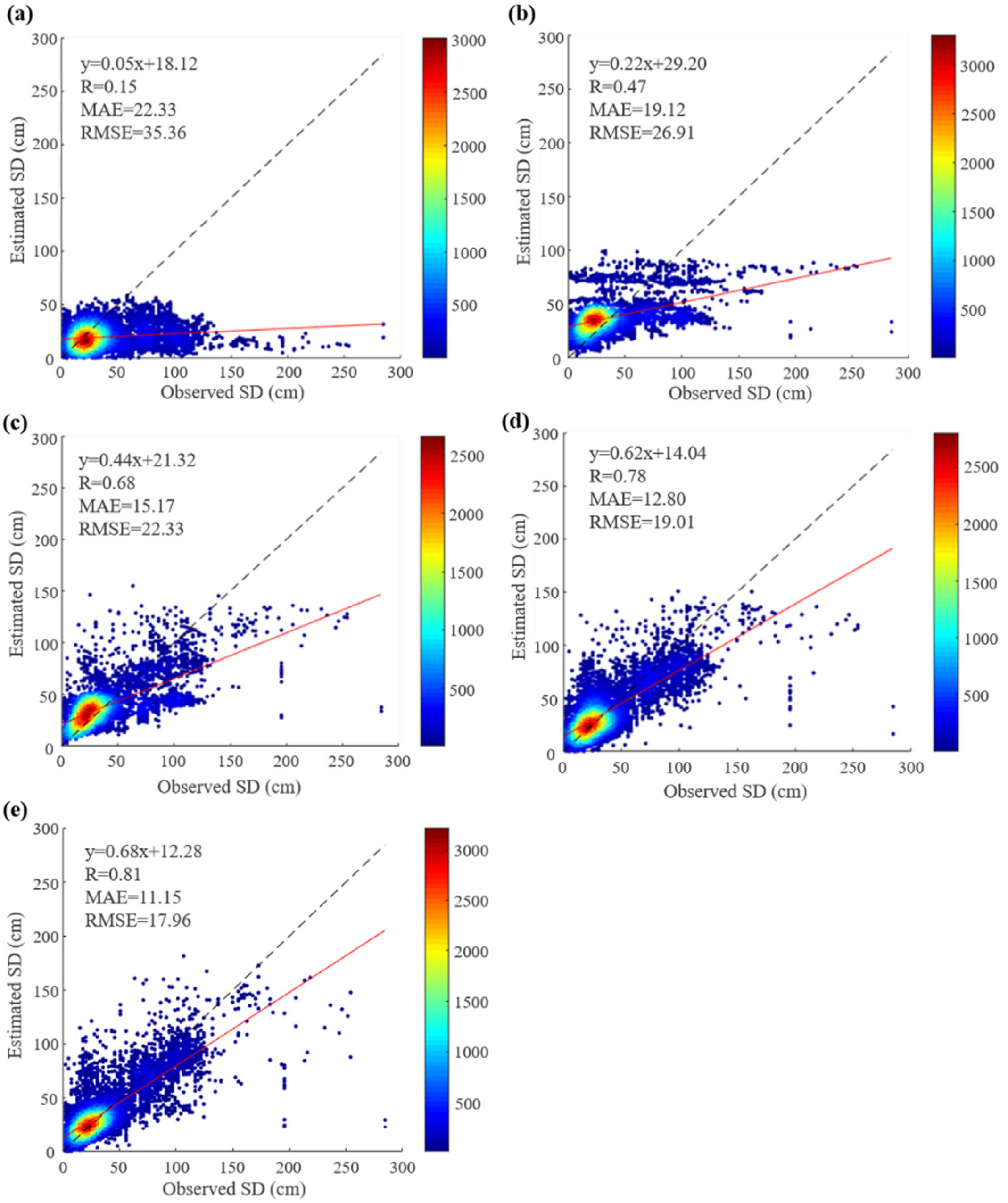

Fig. 8. Scatter plots of the cross-validation results of the five algorithms: (a) Chang; (b) MLR; (c) GRNN; (d) BPNN; (e) DBN.

validation R of 0.76 given its stronger ability for nonlinear mapping.

In summary, the nonlinear methods (BPNN, GRNN, and DBN) are superior to the linear methods, while the proposed DBN SD retrieval model performs the best among all compared models.

4.1.2. *Effect of the added GNSS-R SD estimation*

In this study, GNSS-R SD estimates were taken as the actual SD, together with the in-situ SD data, to increase the station density of the sample data. We compared the results of the models combining satellite observations, in-situ observations, and GNSS-R estimates with those of SD retrieval models combining only satellite observations and in-situ observations, as described in Section 4.1.1, to prove the effect of the addition of GNSS-R estimates.

Table 3 lists the accuracy of the five SD retrieval models combining satellite observations, in-situ observations, and GNSS-R estimates. Fig. 10 presents the scatter plots of the actual SD value and the estimated SD retrieved by the five algorithms. The DBN SD retrieval model and the four models based on combining satellite observations, in-situ observations, and GNSS-R estimates all show higher accuracy in estimating SD than the SD retrieval models based on combining satellite observations and in-situ observations. This result demonstrates that considering the GNSS-R SD estimates to increase the density of the sample data contributes to improving the SD retrieval accuracy. The DBN model also performs best when GNSS-R SD estimates are considered to increase the station density of the sample data. This model has cross-validation R of 0.85, MAE of 9.55 cm, and RMSE of 15.40 cm.

4.2. *Analysis of variations in SD in Alaska*

Based on the proposed DBN SD retrieval model described in Section 4.1.2, the variables of longitude, latitude, elevation, brightness temperature of four channels, the forest cover fraction of each grid cell in Alaska, and time were taken as input data. The daily SD in Alaska from 2008 to 2017 was finally predicted.

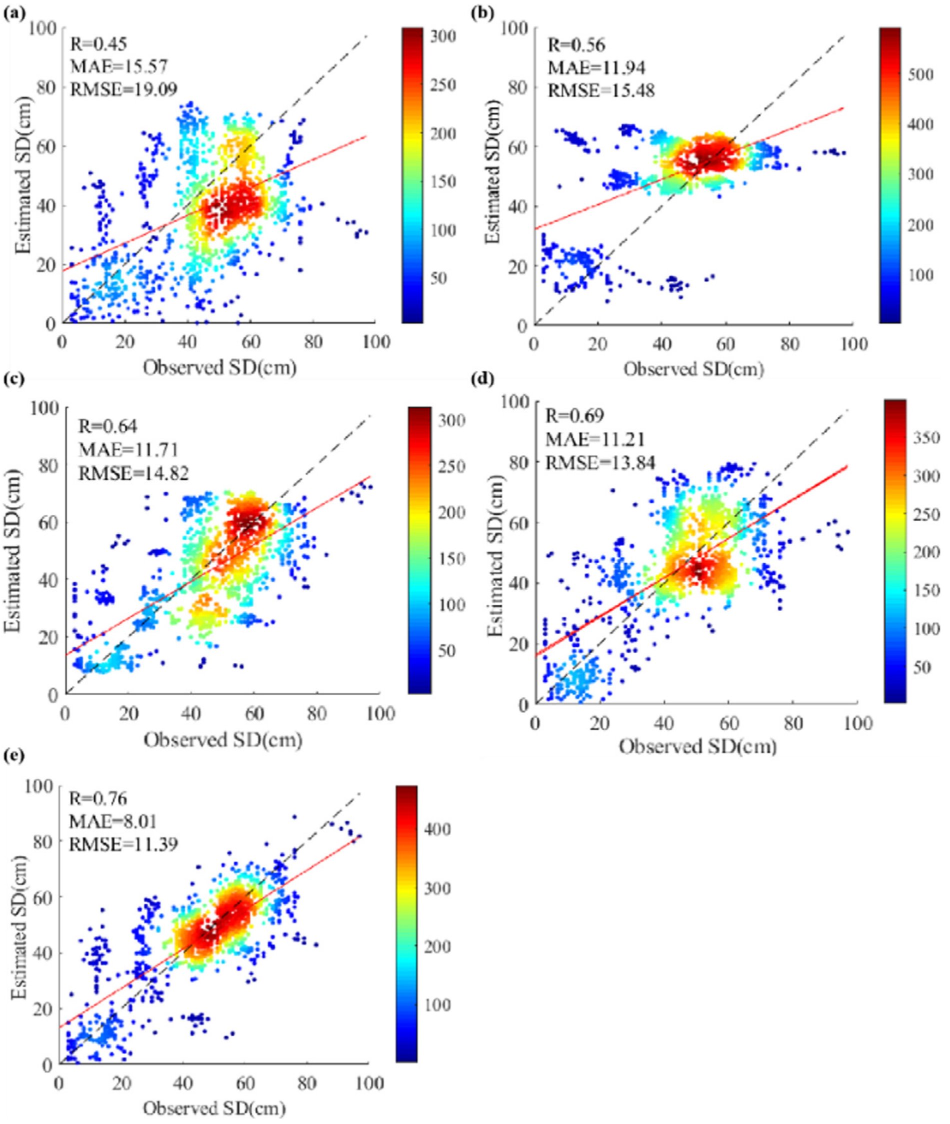

Fig. 9. Scatter plots of the validation results of the five algorithms by using GNSS-R data as independent evaluation data: (a) Chang; (b) MLR; (c) GRNN; (d) BPNN; (e) DBN.

Table 3
Performance of the models using satellite data, in-situ and GNSS-R data.

Method	Model fitting			Cross-validation		
	R	MAE	RMSE	R	MAE	RMSE
Chang (+GNSS-R)				0.20	21.34	33.52
MLR (+GNSS-R)	0.48	17.98	25.68	0.48	17.99	25.66
GRNN (+GNSS-R)	0.75	12.44	19.08	0.72	13.25	20.26
BPNN (+GNSS-R)	0.83	10.33	16.42	0.80	11.35	17.42
DBN (+GNSS-R)	0.87	8.80	14.39	0.85	9.55	15.40

Snow in Alaska is relatively stable from March to April when the SD value nearly reaches the maximum value in a year (Liu et al., 2013). Thus, the mean SD from March to April each year was calculated to analyze the variation in average SD for March and April from 2008 to 2017.

Taking the SD distribution maps of Alaska in 2008 as an example (Fig. 11), it can be seen that the snow of Alaska presents certain spatial distribution characteristics and significant regional differences. The north of Alaska has the greatest SD. This condition may be due to the cold and sub-temperate continental climate of this region. Meanwhile, the overall climate of this region is humid but cold because of its low terrain and closeness to the Arctic Sea. In addition, the average SD in the inland regions is greater than that in the southwest part of Alaska.

The SD anomalies for March and April each year were calculated by subtracting the overall average SD for March and April in this decade (Fig. 12). Red represents an increase in SD, while blue represents a decrease in SD. We can find that from 2011 to 2013, as well as 2009 and 2017, SD anomalies manifest as increase in most area of Alaska, especially in southwest Alaska. In addition, the increase in SD over Alaska was most apparent in 2012. On the contrary, SD anomalies manifest as decrease in most areas of Alaska from 2014 to 2016, as well as 2010.

In the context of global warming, climate anomalies such as El Niño and La Niña would intensify (Ham, 2018). The change in SD during the decade may be a response to the change in temperature and climate anomalies. El Niño occurs when water temperatures in the equatorial sea area of the eastern and central Pacific Ocean continue to warm abnormally, which causes a corresponding change in the global climate. La Niña is the opposite of El Niño and often follows it. El Niño and La Niña greatly influence global climate. Fig. 13a presents the El Niño/Southern Oscillation (ENSO) intensities in the multivariate ENSO index (MEI) during this period, which are available at www.esrl.noaa.gov/

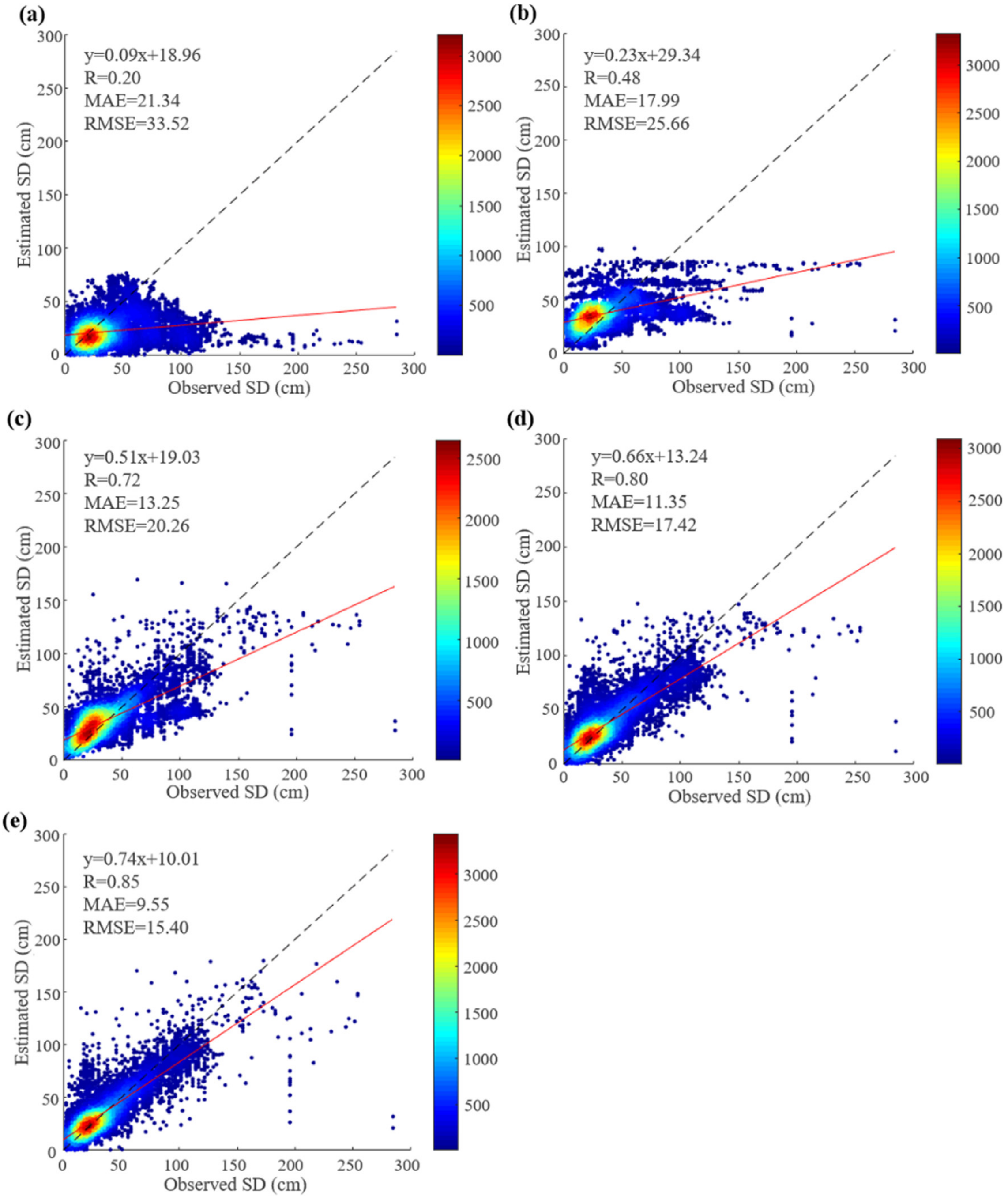

Fig. 10. Scatter plots of the cross-validation results of the five algorithms: (a) Chang; (b) MLR; (c) GRNN; (d) BPNN; (e) DBN.

psd/enso/mei/table.html. Positive MEI values denote El Niño, while negative MEI values indicate La Niña (Wang et al., 2018). Then, the SD anomalies in Fig. 12 were averaged over Alaska for each year and plotted with the ENSO intensities in Fig. 13a. Comparing the change in SD with the occurrence of these climate anomalies (Fig. 13a), we can find that the changes in SD in Alaska have been generally consistent with the climate anomalies over the past decade. From 2008 to 2009 and from 2011 to 2013, as well as 2017, La Niña occurred in March and April, and the SD increased correspondingly. By contrast, from 2014 to 2016, as well as 2010, El Niño occurred, and the SD decreased correspondingly.

The degree of SD change is not completely proportional to the intensity of climate anomalies, especially in 2012, 2013, and 2017. The change in SD may be also related to air temperature, except for the climate anomalies. Air temperature data from NOAA GHCN_CAMS Land Temperature Analysis (https://www.esrl.noaa.gov/psd/data/) were used. The air temperature anomalies for March and April each year in this decade were averaged over Alaska and shown with the mean SD anomalies in Fig. 13b. We can find that in 2013, La Niña was weak, and correspondingly, the increase in SD anomalies should be small. However, the significant decrease in air temperature in 2013 resulted in a larger increase in SD. The case in 2017 is also similar to that in 2013. Besides, the La Niña phenomenon was stronger in 2011 than in 2012, but due to the air temperature was lower in 2012, resulting in the SD in 2012 larger than that in 2011. Therefore, the change in SD is mainly affected by the combination of the change in temperature and climate anomalies. In addition to the influence of climate anomalies and temperature, some other factors that may affect the change in SD, such as

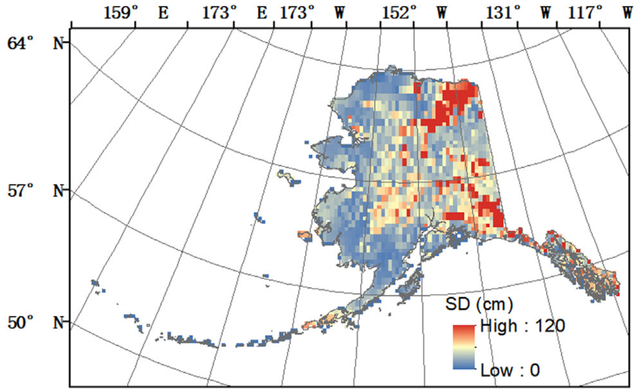

Fig. 11. Distribution of the average SD for March and April in 2008 over Alaska.

ocean currents and terrain, etc., require further discussion.

5. Conclusions

In this study, we innovatively introduced a deep learning network to improve the precision of satellite-derived SD. In addition, high-precision GNSS-R SD product data were utilized as the actual value of the SD, together with ground-measured SD data, to increase the station density of the sample data. The results showed that the DBN SD retrieval model estimates SD more accurately than linear methods and conventional neural network models. Furthermore, the effectiveness of combining GNSS-R estimates for increasing the station density of the sample data was demonstrated. Specifically, R increased from 0.81 to 0.85, MAE decreased from 11.15 cm to 9.55 cm, and RMSE decreased from 17.96 cm to 15.40 cm. Finally, the daily SD over the whole of Alaska was predicted using the proposed DBN SD retrieval model. The results displayed that the variation in SD for March and April between 2008 and 2017 in Alaska is mainly associated with the occurrence of climate anomalies and the change in air temperature over this time period.

There is still room for improvement of the proposed approach and for further study. On the one hand, the current spatial resolution of estimated SD is coarse (25 km × 25 km), which would limit its application in operational hydrological modeling and snow-caused disaster monitoring. Thus, enhancing the spatial resolution of the SD data is required. On the other hand, we only applied a deep learning network (the DBN model) to establish the relationship between brightness temperature and SD. Whether other deep learning models can better handle this issue is worth investigating.

CRediT authorship contribution statement

Jiwen Wang: Conceptualization, Methodology, Software, Investigation, Data curation, Writing - original draft. **Qiangqiang Yuan:** Conceptualization, Methodology, Validation, Visualization, Formal analysis, Writing - review & editing. **Huanfeng Shen:** Formal analysis, Supervision, Writing - review & editing. **Tingting Liu:**

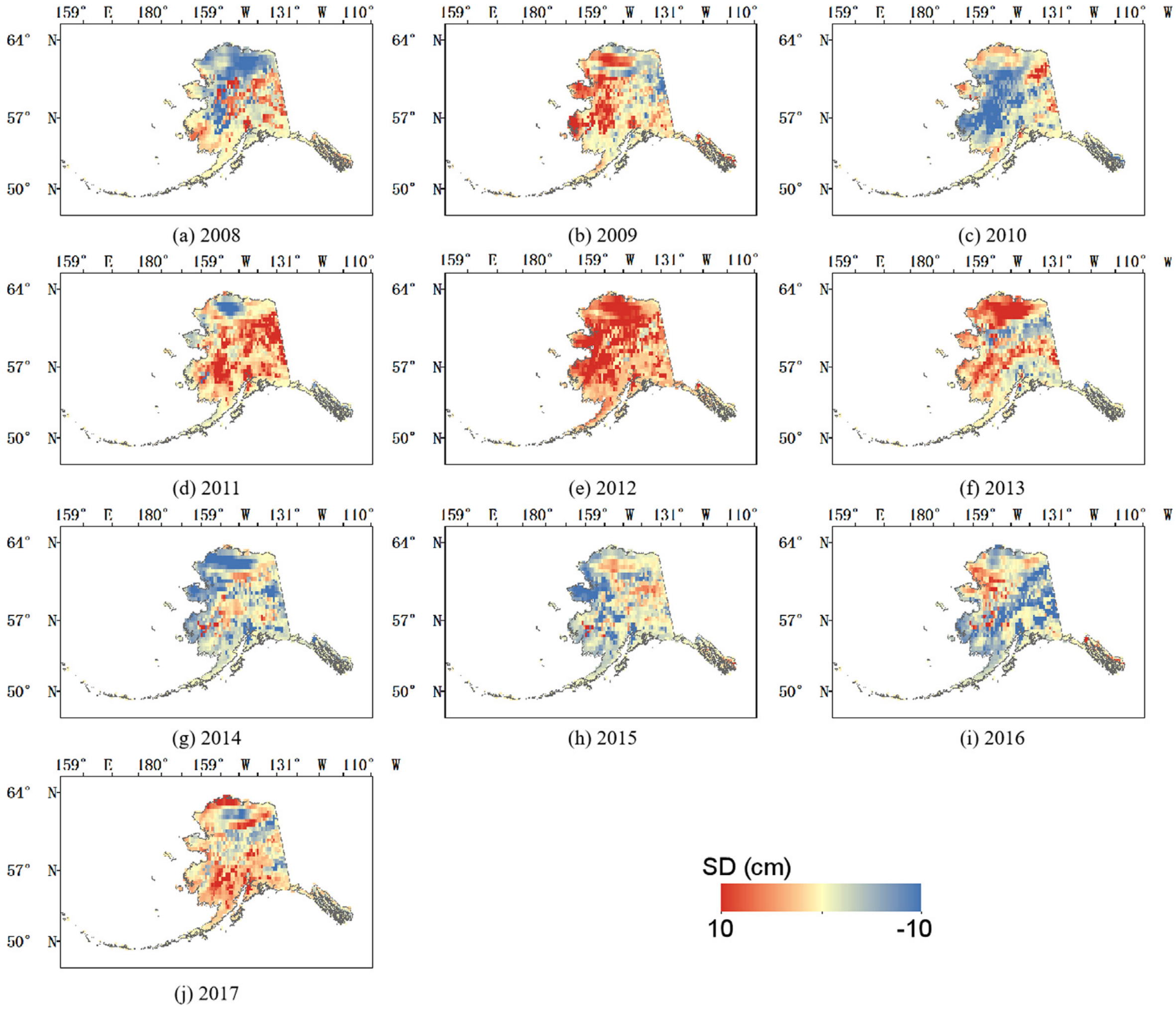

(a) 2008
(b) 2009
(c) 2010
(d) 2011
(e) 2012
(f) 2013
(g) 2014
(h) 2015
(i) 2016
(j) 2017

Fig. 12. SD anomalies for March and April each year from 2008 to 2017.

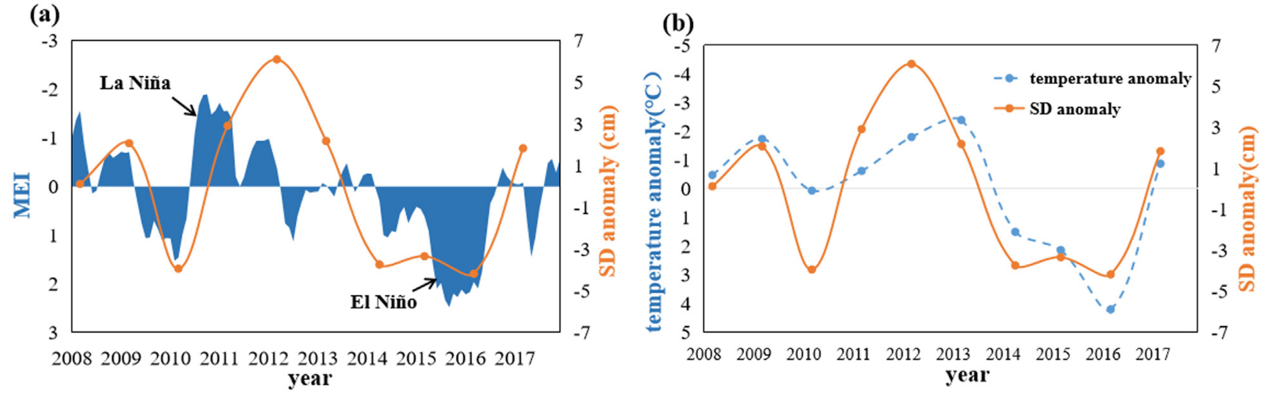

Fig. 13. ENSO intensities in MEI, mean SD anomaly, and mean air temperature anomaly for March and April from 2008 to 2017. (a) ENSO intensities in MEI and mean SD anomaly for March and April from 2008 to 2017. (b) Mean SD anomaly and mean air temperature anomaly for March and April from 2008 to 2017.

Visualization, Writing - review & editing. **Tongwen Li:** Software, Writing - review & editing. **Linwei Yue:** Resources, Writing - review & editing. **Xiaogang Shi:** Writing - review & editing. **Liangpei Zhang:** Writing - review & editing.

Declaration of Competing Interest

The authors declare that they have no known competing financial interests or personal relationships that could have appeared to influence the work reported in this paper.

Acknowledgments

We gratefully acknowledge the support from the Strategic Priority Research Program of the Chinese Academy of Sciences (No. XDA19090104), the National Natural Science Foundation of China (Nos. 41922008 and 41676179), and the Fundamental Research Funds for the Central Universities of Wuhan University (No. 2042019kf0213). The authors would also like to thank the National Snow and Ice Data Center for providing the SSMIS brightness temperature data. The in-situ SD data were obtained from the Global Historical Climate Network. The GNSS-R SD were sourced from the PBO H2O Data Portal. The MODIS VCF data were obtained from LAADS DAAC. The ETOPO1 data were obtained from the National Geophysical Data Center of NOAA. The temperature analysis data were acquired from NOAA ESRL PSD.

References

Amante, C., Eakins, B.W., 2009. ETOPO1 arc-minute global relief model: procedures, data sources and analysis.
Armstrong, R., Knowles, K., Brodzik, M., Hardman, M., 1994. DMSP SSM/I-SSMIS pathfinder daily EASE-grid brightness temperatures. Version 2. NASA National Snow Ice Data Center Distributed Active Archive Center: Boulder, CO, USA.
Armstrong, R.L., Brodzik, M.J., 2002. Hemispheric-scale comparison and evaluation of passive-microwave snow algorithms. Ann. Glaciol. 34, 38–44.
Bair, E.H., Abreu Calfa, A., Rittger, K., Dozier, J., 2018. Using machine learning for real-time estimates of snow water equivalent in the watersheds of Afghanistan. Cryosphere 12.
Boniface, K., Braun, J., McCreight, J., Nievinski, F., 2015. Comparison of snow data assimilation system with GPS reflectometry snow depth in the western United States. Hydrol. Process. 29, 2425–2437.
Brodzik, M.J., 2002. EASE-Grid: A versatile set of equal-area projections and grids. Discrete global grids.
Cao, Y., Yang, X., Zhu, X., 2008. Retrieval snow depth by artificial neural network methodology from integrated AMSR-E and in-situ data—a case study in Qinghai-Tibet Plateau. Chinese Geograph. Sci. 18, 356–360.
Chang, A., Foster, J., Hall, D.K., 1987. Nimbus-7 SMMR derived global snow cover parameters. Ann. Glaciol. 9, 39–44.
Chang, A., Tsang, L., 1992. A neural network approach to inversion of snow water equivalent from passive microwave measurements. Hydrol. Res. 23, 173–182.
Che, T., Dai, L., Zheng, X., Li, X., Zhao, K., 2016. Estimation of snow depth from passive microwave brightness temperature data in forest regions of northeast China. Remote Sens. Environ. 183, 334–349.
Che, T., Li, X., Jin, R., Armstrong, R., Zhang, T., 2008. Snow depth derived from passive microwave remote-sensing data in China. Ann. Glaciol. 49, 145–154.
Chen, Y., Zhao, X., Jia, X., 2015. Spectral–spatial classification of hyperspectral data based on deep belief network. IEEE J. Sel. Top. Appl. Earth Obs. Remote Sens. 8, 2381–2392.
Dai, L., Che, T., Wang, J., Zhang, P., 2012. Snow depth and snow water equivalent estimation from AMSR-E data based on a priori snow characteristics in Xinjiang, China. Remote Sens. Environ. 127, 14–29.
Davis, D.T., Chen, Z., Tsang, L., Hwang, J.-N., Chang, A.T., 1993. Retrieval of snow parameters by iterative inversion of a neural network. IEEE Trans. Geosci. Remote Sens. 31, 842–852.
Dietz, A.J., Kuenzer, C., Gessner, U., Dech, S., 2012. Remote sensing of snow–a review of available methods. Int. J. Remote Sens. 33, 4094–4134.
Evora, N.D., Tapsoba, D., De Seve, D., 2008. Combining artificial neural network models, geostatistics, and passive microwave data for snow water equivalent retrieval and mapping. IEEE Trans. Geosci. Remote Sens. 46, 1925–1939.
Foster, J., Chang, A., Hall, D., 1997. Comparison of snow mass estimates from a prototype passive microwave snow algorithm, a revised algorithm and a snow depth climatology. Remote Sens. Environ. 62, 132–142.
Gan, T.Y., Barry, R.G., Gizaw, M., Gobena, A., Balaji, R., 2013. Changes in North American snowpacks for 1979–2007 detected from the snow water equivalent data of SMMR and SSM/I passive microwave and related climatic factors. J. Geophys. Res.: Atmospheres 118, 7682–7697.
Gan, T.Y., Kalinga, O., Singh, P., 2009. Comparison of snow water equivalent retrieved from SSM/I passive microwave data using artificial neural network, projection pursuit and nonlinear regressions. Remote Sens. Environ. 113, 919–927.
Grody, N.C., Basist, A.N., 1996. Global identification of snowcover using SSM/I measurements. IEEE Trans. Geosci. Remote Sens. 34, 237–249.
Gu, L., Ren, R., Zhao, K., Li, X., 2014. Snow depth and snow cover retrieval from FengYun3B microwave radiation imagery based on a snow passive microwave unmixing method in Northeast China. J. Appl. Remote Sens. 8, 084682.
Ham, Y.-G., 2018. El Niño events will intensify under global warming. In: Nature Publishing Group.
Hinton, G.E., Osindero, S., Teh, Y.-W., 2006. A fast learning algorithm for deep belief nets. Neural Comput. 18, 1527–1554.
Hinton, G.E., Salakhutdinov, R.R., 2006. Reducing the dimensionality of data with neural networks. Science 313, 504–507.
Hu, X., Waller, L.A., Al-Hamdan, M.Z., Crosson, W.L., Estes Jr, M.G., Estes, S.M., Quattrochi, D.A., Sarnat, J.A., Liu, Y., 2013. Estimating ground-level PM2. 5 concentrations in the southeastern US using geographically weighted regression. Environ. Res. 121, 1–10.
Huang, W., Song, G., Hong, H., Xie, K., 2014. Deep architecture for traffic flow prediction: deep belief networks with multitask learning. IEEE Trans. Intell. Transp. Syst. 15, 2191–2201.
Jia, Y., Jin, S., Savi, P., Gao, Y., Tang, J., Chen, Y., Li, W., 2019. GNSS-R soil moisture retrieval based on a XGboost machine learning aided method: Performance and validation. Remote Sens. 11, 1655.
Kang, D.H., Shi, X., Gao, H., Déry, S.J., 2014. On the changing contribution of snow to the hydrology of the Fraser River Basin, Canada. J. Hydrometeorol. 15, 1344–1365.
Kelly, R.E., Chang, A.T., 2003. Development of a passive microwave global snow depth retrieval algorithm for Special Sensor Microwave Imager (SSM/I) and Advanced Microwave Scanning Radiometer-EOS (AMSR-E) data. Radio Sci. 38 41-41-41-11.
Langlois, A., Royer, A., Dupont, F., Roy, A., Goita, K., Picard, G., 2011. Improved corrections of forest effects on passive microwave satellite remote sensing of snow over boreal and subarctic regions. IEEE Trans. Geosci. Remote Sens. 49, 3824–3837.
Larson, K.M., Gutmann, E.D., Zavorotny, V.U., Braun, J.J., Williams, M.W., Nievinski, F.G., 2009. Can we measure snow depth with GPS receivers? Geophys Res. Lett. 36.
Larson, K.M., Nievinski, F.G., 2013. GPS snow sensing: results from the earthscope plate boundary observatory. GPS Solut. 17, 41–52.
Li, L., Chen, H., Guan, L., 2019. Retrieval of snow depth on sea ice in the arctic using the FengYun-3B microwave radiation imager. J. Ocean Univ. China 18, 580–588.
Li, T., Shen, H., Yuan, Q., Zhang, X., Zhang, L., 2017. Estimating ground-level PM2. 5 by fusing satellite and station observations: a geo-intelligent deep learning approach. Geophys. Res. Lett. 44 11,985–911,993.

Liu, X., Jiang, L., Wang, G., Hao, S., Chen, Z., 2018. Using a linear unmixing method to improve passive microwave snow depth retrievals. IEEE J. Sel. Top. Appl. Earth Obs. Remote Sens. 11, 4414–4429.

Liu, Y., Peters-Lidard, C.D., Kumar, S., Foster, J.L., Shaw, M., Tian, Y., Fall, G.M., 2013. Assimilating satellite-based snow depth and snow cover products for improving snow predictions in Alaska. Adv. Water Resour. 54, 208–227.

Mashtayeva, S., Dai, L., Che, T., Sagintayev, Z., Sadvakasova, S., Kussainova, M., Alimbayeva, D., Akynbekkyzy, M., 2016. Spatial and temporal variability of snow depth derived from passive microwave remote sensing data in Kazakhstan. J. Meteorol. Res. 30, 1033–1043.

McCreight, J.L., Small, E.E., Larson, K.M., 2014. Snow depth, density, and SWE estimates derived from GPS reflection data: validation in the western US. Water Resour. Res. 50, 6892–6909.

Nievinski, F.G., Larson, K.M., 2014. Inverse modeling of GPS multipath for snow depth estimation—Part II: Application and validation. IEEE Trans. Geosci. Remote Sens. 52, 6564–6573.

Rasmussen, R., Baker, B., Kochendorfer, J., Meyers, T., Landolt, S., Fischer, A.P., Black, J., Thériault, J.M., Kucera, P., Gochis, D., 2012. How well are we measuring snow: The NOAA/FAA/NCAR winter precipitation test bed. Bull. Am. Meteorol. Soc. 93, 811–829.

Rodriguez, J.D., Perez, A., Lozano, J.A., 2010. Sensitivity analysis of k-fold cross validation in prediction error estimation. IEEE Trans. Pattern Anal. Machine Intelligence 32, 569–575.

Rosenfeld, S., Grody, N., 2000. Anomalous microwave spectra of snow cover observed from Special Sensor Microwave/Imager measurements. J. Geophys. Res.: Atmospheres 105, 14913–14925.

Rostosky, P., Spreen, G., Farrell, S.L., Frost, T., Heygster, G., Melsheimer, C., 2018. Snow depth retrieval on Arctic sea ice from passive microwave radiometers—improvements and extensions to multiyear ice using lower frequencies. J. Geophys. Res. Oceans 123, 7120–7138.

Rumelhart, D.E., Hinton, G.E., Williams, R.J., 1988. Learning representations by back-propagating errors. Cognitive Model. 5, 1.

Santi, E., Pettinato, S., Paloscia, S., Pampaloni, P., Fontanelli, G., Crepaz, A., Valt, M., 2014. Monitoring of Alpine snow using satellite radiometers and artificial neural networks. Remote Sens. Environ. 144, 179–186.

Santi, E., Pettinato, S., Paloscia, S., Pampaloni, P., Macelloni, G., Brogioni, M., 2012. An algorithm for generating soil moisture and snow depth maps from microwave spaceborne radiometers: HydroAlgo. Hydrol. Earth Syst. Sci. 16 (10), 3659–3676.

Shi, J., Xiong, C., Jiang, L., 2016. Review of snow water equivalent microwave remote sensing. Science China Earth Sciences 59, 731–745.

Shi, X., Marsh, P., Yang, D., 2015. Warming spring air temperatures, but delayed spring streamflow in an Arctic headwater basin. Environ. Res. Lett. 10, 064003.

Singh, P.R., Gan, T.Y., 2000. Retrieval of snow water equivalent using passive microwave brightness temperature data. Remote Sens. Environ. 74, 275–286.

Song, X., Zhang, G., Liu, F., Li, D., Zhao, Y., Yang, J., 2016. Modeling spatio-temporal distribution of soil moisture by deep learning-based cellular automata model. J. Arid Land 8, 734–748.

Specht, D.F., 1991. A general regression neural network. IEEE Trans. Neural Networks 2, 568–576.

Tabari, H., Marofi, S., Abyaneh, H.Z., Sharifi, M., 2010. Comparison of artificial neural network and combined models in estimating spatial distribution of snow depth and snow water equivalent in Samsami basin of Iran. Neural Comput. Appl. 19, 625–635.

Tabibi, S., Geremia-Nievinski, F., van Dam, T., 2017. Statistical comparison and combination of GPS, GLONASS, and multi-GNSS multipath reflectometry applied to snow depth retrieval. IEEE Trans. Geosci. Remote Sens. 55, 3773–3785.

Tedesco, M., Derksen, C., Deems, J.S., Foster, J.L., 2015. Remote sensing of snow depth and snow water equivalent. Remote Sens. Cryosphere 73–98.

Tedesco, M., Pulliainen, J., Takala, M., Hallikainen, M., Pampaloni, P., 2004. Artificial neural network-based techniques for the retrieval of SWE and snow depth from SSM/I data. Remote Sens. Environ. 90, 76–85.

Tsutsui, H., Maeda, T., 2017. Possibility of estimating seasonal snow depth based solely on passive microwave remote sensing on the greenland ice sheet in Spring. Remote Sens. 9, 523.

Ulaby, F.T., Stiles, W.H., 1980. The active and passive microwave response to snow parameters: 2. Water equivalent of dry snow. J. Geophys. Res. Oceans 85, 1045–1049.

Vey, S., Güntner, A., Wickert, J., Blume, T., Thoss, H., Ramatschi, M., 2016. Monitoring snow depth by GNSS Reflectometry in built-up areas: a case study for Wettzell, Germany. IEEE J. Sel. Top. Appl. Earth Obs. Remote Sens. 9, 4809–4816.

Wang, J., Song, C., Reager, J.T., Yao, F., Famiglietti, J.S., Sheng, Y., MacDonald, G.M., Brun, F., Schmied, H.M., Marston, R.A., 2018. Recent global decline in endorheic basin water storages. Nat. Geosci. 11, 926–932.

Wang, W., Huang, X., Deng, J., Xie, H., Liang, T., 2015. Spatio-temporal change of snow cover and its response to climate over the Tibetan Plateau based on an improved daily cloud-free snow cover product. Remote Sens. 7, 169–194.

Wu, X., Che, T., Li, X., Wang, N., Yang, X., 2018. Slower snowmelt in spring along with climate warming across the Northern Hemisphere. Geophys. Res. Lett. 45 12,331–312,339.

Xiao, X., Zhang, T., Zhong, X., Shao, W., Li, X., 2018. Support vector regression snow-depth retrieval algorithm using passive microwave remote sensing data. Remote Sens. Environ. 210, 48–64.

Xu, H., Yuan, Q., Li, T., Shen, H., Zhang, L., Jiang, H., 2018. Quality improvement of satellite soil moisture products by fusing with in-situ measurements and GNSS-R estimates in the western continental US. Remote Sens. 10, 1351.

Zhang, S., Wang, X., Zhang, Q., 2017. Avoiding errors attributable to topography in GPS-IR snow depth retrievals. Adv. Space Res. 59, 1663–1669.